JOURNAL OF SYNCHROTRON RADIATION

ISSN 1600-5775

Two-stage reflective self-seeding scheme for high-repetition-rate X-ray free-electron lasers

Guanqun Zhou,[a,b,c] Zhengxian Qu,[a,d] Yanbao Ma,[d] William J. Corbett,[a] Yi Jiao,[b,c] Haoyuan Li,[a] Weilun Qin,[e] Tor O. Raubenheimer,[a] Cheng-Ying Tsai,[f] Jiuqing Wang,[b,c] Chuan Yang[g] and Juhao Wu[a]*

[a]SLAC National Accelerator Laboratory, Stanford University, Stanford, CA 94309, USA, [b]Key Laboratory of Particle Acceleration Physics and Technology, Institute of High Energy Physics, Chinese Academy of Sciences, Beijing 100049, People's Republic of China, [c]University of Chinese Academy of Sciences, Beijing 100049, People's Republic of China, [d]Department of Mechanical Engineering, University of California Merced, Merced, CA 95343, USA, [e]Department of Physics, Lund University, PO Box 118, Lund 22100, Sweden, [f]State Key Laboratory of Advanced Electromagnetic Engineering and Technology, School of Electrical and Electronic Engineering, Huazhong University of Science and Technology, Wuhan 430074, People's Republic of China, and [g]School of Physical Science and Technology, ShanghaiTech University, 201210 Shanghai, People's Republic of China. *Correspondence e-mail: jhwu@slac.stanford.edu

Received 11 April 2020
Accepted 9 November 2020

Edited by M. Yabashi, RIKEN SPring-8 Center, Japan

Keywords: self-seeding free-electron laser; crystal monochromator; thermomechanical effects; high repetition rate; narrow bandwidth.

X-ray free-electron lasers (XFELs) open a new era of X-ray based research by generating extremely intense X-ray flashes. To further improve the spectrum brightness, a self-seeding FEL scheme has been developed and demonstrated experimentally. As the next step, new-generation FELs with high repetition rates are being designed, built and commissioned around the world. A high repetition rate would significantly speed up the scientific research; however, alongside this improvement comes new challenges surrounding thermal management of the self-seeding monochromator. In this paper, a new configuration for self-seeding FELs is proposed, operated under a high repetition rate which can strongly suppress the thermal effects on the monochromator and provides a narrow-bandwidth FEL pulse. Three-dimension time-dependent simulations have been performed to demonstrate this idea. With this proposed configuration, high-repetition-rate XFEL facilities are able to generate narrow-bandwidth X-ray pulses without obvious thermal concern on the monochromators.

1. Introduction

The free-electron laser (FEL) opens the door to a new frontier of high-intensity X-ray experiments in various research fields, *e.g.* physics (Young *et al.*, 2010), chemistry (Zhang *et al.*, 2014), life (Seibert *et al.*, 2011) and material sciences (Milathianaki *et al.*, 2013). Combined with ultra-short duration, refined spatial resolution and high photon flux, hard X-ray FELs have become powerful tools to capture simultaneous information on atomic structure and dynamics, which have been exemplified by the successful operation of various X-ray FEL sources (Emma *et al.*, 2010; Ishikawa *et al.*, 2012; Kang *et al.*, 2017; Decking *et al.*, 2020), *e.g.* the Linac Coherent Light Source (LCLS). The process of X-ray generation in these machines is based on self-amplified spontaneous emission (SASE) (Kondratenko & Saldin, 1980; Bonifacio *et al.*, 1984), in which the electron beam spontaneous emission is amplified during the continuous interaction while the electron beam is traveling through the undulators. The X-rays produced in the SASE process are transversely coherent; however, due to the stochastic nature of this process, one cannot fully utilize the electron beam to generate photons all in a narrow bandwidth (Andruszkow *et al.*, 2000; Wu *et al.*, 2010; Zhou *et al.*, 2020).

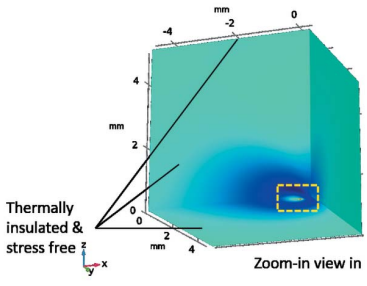

One efficient way to improve the X-ray temporal properties is the self-seeding technique, which has been demonstrated experimentally at LCLS (Amann *et al.*, 2012). With an inserted transmissive monochromator in the undulator system, the SASE FEL spectrum is filtered and a narrow-bandwidth wake seed is generated. Then, the narrow bandwidth seed will be amplified in the later undulator segments. In this way, the self-seeding scheme improves the FEL spectrum brightness dramatically. Naturally, the 'seed' property has a strong dependence on the monochromator properties, *e.g.* the material, the atomic reflection layer, inner strain field (bending, temperature field, *etc.*). Next-generation FEL facilities, like European XFEL, LCLS-II (Decking *et al.*, 2020; Emma *et al.*, 2014), are employing superconducting technology to improve the repetition rate (X-ray pulse per second) to the MHz level, to speed up the scientific discoveries utilizing the FEL pulses. Alongside these advances, these high-repetition-rate machines will bring new challenges on the thermal management of the self-seeding monochromator. Due to the ultra-short duration of FEL pulses, the self-seeding monochromator would be heated up instantaneously. This sudden temperature change will induce local strain and elastic waves (Yang *et al.*, 2018*a*). For a low-repetition machine, there is enough time for the monochromator to recover. But for the high-repetition machines, there is not enough time for the monochromator to recover before the next FEL pulse arrives. Strain field induced by this thermal effect would lead to seed property degradation, *e.g.* bandwidth broadening, central photon energy shift (Qu *et al.*, 2020*a*).

With regard to this issue, various studies on monochromator thermal control and self-seeding scheme design, *e.g.* two-stage transmissive self-seeding, have been carried out (Liu *et al.*, 2019; Samoylova *et al.*, 2019; Yang *et al.*, 2018*b*; Geloni *et al.*, 2011). Meanwhile, recently, it has been demonstrated that reflective self-seeding schemes can be used to generate Fourier transform limited FEL pulses (Inoue *et al.*, 2019). Instead of using the forward Bragg diffraction as the seed, the reflective self-seeding scheme employs a micro channel-cut monochromator as the bandwidth filter and utilizes Bragg diffraction as the seed. Inspired by this success and the configuration of two-stage transmissive self-seeding, we propose a scheme that distributes the thermal load on two reflective, silicon micro channel-cut monochromators with different atomic layers for reflection: a two-stage reflective self-seeding (TRSS) scheme. Hence, the thermal effects on each monochromator would be reduced. Based on this configuration, using three-dimensional time-dependent FEL simulation, we successfully demonstrated that it is possible to generate high-repetition-rate narrow bandwidth X-ray pulses.

2. Two-stage reflective self-seeding scheme

In a FEL, a bunch of highly relativistic electrons are injected into a periodically varying magnetic field, known as an undulator. While traveling through the undulator, the electrons are forced to wiggle transversely and emit spontaneous radiation. This process produces ultra-short bursts of X-rays at the wavelengths

$$\lambda_r = \frac{\lambda_u}{2\gamma_0^2}\left(1 + a_u^2\right), \tag{1}$$

where λ_u is the undulator period, γ_0 is the electron beam Lorentz factor, and a_u is the RMS undulator parameter.

Generally, this process can be described with the well known one-dimensional model analytically. Universally scaled collective variables are induced to describe the FEL dynamics (Bonifacio *et al.*, 1984). The normalized radiation field is defined as $A = E/(4\pi mc^2\gamma\rho n_e)^{1/2}$ where E is the radiation field, m is the electron mass, c is the speed of light, n_e is the electron beam density, and $\rho = (a_u\omega_p/4ck_u)^{2/3}/\gamma$ is the Pierce parameter, with $\omega_p = (4\pi e^2 n_e/m)^{1/2}$, the plasma frequency and $k_u = 2\pi/\lambda_u$, the undulator wavenumber. The bunching factor is defined as

$$B = \frac{1}{N_\lambda}\sum_{j=1}^{N_\lambda}\exp\left(-i\theta_j\right),$$

where $\theta_j = (k_u + k_r)z - ck_r t_j$ is the ponderomotive phase, k_r is the radiation wavenumber, z is the coordinate along the undulator axis, t_j is time, and N_λ is the number of electrons within one radiation wavelength λ_r. A high-gain FEL process can be described by

$$\begin{aligned}\frac{\partial A(\overline{z},\overline{z}_1)}{\partial\overline{z}} + \frac{\partial A(\overline{z},\overline{z}_1)}{\partial\overline{z}_1} &= B(\overline{z},\overline{z}_1) + i\delta A(\overline{z},\overline{z}_1)\\ \frac{\partial^2 B(\overline{z},\overline{z}_1)}{\partial\overline{z}^2} &= iA(\overline{z},\overline{z}_1),\end{aligned} \tag{2}$$

where the normalized coordinate variables are introduced, $\delta = (\gamma - \gamma_0)/\gamma_0$, the relative energy spread, $\overline{z} = z/l_g$, with $l_g = \lambda_u/4\pi\rho$, the gain length and $\overline{z}_1 = -c(t - z/v_z)/l_c$, with $l_c = \lambda_r/4\pi\rho$, the cooperation length. The solution in the spectrum domain can be expressed as

$$a(\overline{z},\overline{\omega}) = b(0,\overline{\omega})\,g(\overline{z},\overline{\omega}) + a(0,\overline{\omega})\,g'(\overline{z},\overline{\omega}), \tag{3}$$

where the prime indicates the derivative with respect to $\overline{z}$, $b(0,\overline{\omega})$ and $a(0,\overline{\omega})$ are the Fourier transforms of the initial bunching $B(0,\overline{z}_1)$ and the input signal $A(0,\overline{z}_1)$, and $g(\overline{z},\overline{\omega})$ is defined as

$$g(\overline{z},\overline{\omega}) = -i\sum_{j=1}^{3}\frac{\exp\left[i\nu_j(\overline{\omega})\,\overline{z}\right]}{3\nu_j(\overline{\omega}) - 2(\delta + \overline{\omega})}, \tag{4}$$

and $\overline{\omega}$ are the solutions of the cubic equation $\nu^3 - (\delta + \overline{\omega})\nu^2 + 1 = 0$ (Bonifacio *et al.*, 1994). Here, $g(\overline{z},\overline{\omega})$ and $g'(\overline{z},\overline{\omega})$ describe the exponential gain of the FEL in the high-gain regime.

The emitted field spectrum $a(\overline{z},\overline{\omega})$ consists of two terms. One, proportional to the initial bunching of the electron beam, $b(0,\overline{\omega})$, describes the SASE regime, and the other, proportional to the initial field $a(0,\overline{\omega})$, describes the seed amplification. They are in a linear competition. In the self-seeding scheme, we have to guarantee that the seed amplification effect is much stronger than the SASE to keep the spectrum clean during the FEL gain.

In a self-seeding scheme, the crystal monochromator can be well described by the theory of dynamic diffraction (Shvyd'ko & Lindberg, 2012; Lugovskaya & Stepanov, 1991). Based on this, one can calculate the frequency filter of a micro channel-cut monochromator. Then, the relation between the output seed and input pulse can be described as

$$a_{\rm out}(\overline{\omega}) = a_{\rm in}(\overline{\omega})\, R_{\rm mono}(\overline{\omega}), \tag{5}$$

where $R_{\rm mono}(\overline{\omega})$, a complex function of $\overline{\omega}$, describes the X-ray diffraction effects of frequency filtering. Then, the X-ray absorption by the monochromator can be calculated with

$$I_{\rm abp}(\overline{\omega}) = I_{\rm in}(\overline{\omega})\Big[1 - \left|R_{\rm mono}(\overline{\omega})\right|^2 - \left|T_{\rm mono}(\overline{\omega})\right|^2\Big], \tag{6}$$

where $T_{\rm mono}(\overline{\omega})$ describes the forward X-ray diffraction effects.

Fig. 1 illustrates the configuration of the TRSS scheme and depicts in essence how it works. Similar to two-stage transmissive self-seeding scheme (Liu *et al.*, 2019; Geloni *et al.*, 2011; Yang *et al.*, 2018*b*), the whole undulator system is split into three segments separated by two components each containing a micro channel-cut monochromator, a chicane and a dogleg. A SASE FEL pulse with sufficient power will be generated in the first segment of undulators. The first micro channel-cut monochromator is used to preliminarily purify the X-ray spectrum. After that, the seed signal will be amplified in the second segment of undulators and be further purified by the second micro channel-cut monochromator. Finally, the seed signal will be further amplified in the third segment of undulators. As illustrated in Fig. 1, the micro channel-cut monochromator will induce a transverse shift (shown in side view) and a delay (shown in top view) between the X-ray pulse and the electron beam. Similar to the reflective self-seeding scheme (Inoue *et al.*, 2019), to compensate for the delay, we use a chicane to generate an electron beam bypass to synchronize it with the X-ray pulse and employ a dogleg to induce a transverse shift to align the electron beam with the X-ray pulse.

The SASE generation in the first undulator section can be modeled as the case that $a(0, \overline{\omega}) = 0$ in equation (3). Then at the first reflective mono, the SASE spectrum will be purified. Since the chicane would wash out the microbunching in the electron beam which is still relatively 'fresh' (with good quality), for the next section, we can approximately model it as a seeded high-gain FEL process with $a(0, \overline{\omega}) \gg b(0, \overline{\omega})$. This means that the seed can dominate the electron beam shot noise which triggers the SASE process. Then the signal amplified by the second section will be further purified by the second reflective mono and the so-produced signal will drive the FEL gain in the final undulator section.

It is worthwhile to mention that the energy absorbed by a reflective monochromator depends on two factors: (1) the FEL pulse energy and (2) the ratio between the Darwin width of the crystal and the bandwidth of the input pulse. Assuming that the input FEL pulse bandwidth is fixed, if the Darwin width of the crystal is wider, the absorption ratio (the ratio between absorbed energy and input pulse energy) will be lower, since a larger fraction of the spectrum has been reflected. This leads to higher seeding efficiency, and vice versa. Of course, if the absorption ratio is fixed, higher pulse energy means higher absorption. Base on this, by subtly choosing the atomic layer and undulator length in each segment, we can make the first monochromator (working with SASE pulses) have a wider bandwidth, higher seeding efficiency and lower absorption ratio, which helps to reduce the absorption on the first monochromator. For the second monochromator, since the input pulse is already narrow-bandwidth, a further bandwidth reduction will not raise a thermal issue. This idea provides a way to balance the heat load on each monochromator.

3. Simulation

In this section, we are going to investigate the performance of this TRSS scheme by three-dimensional (3D) time-dependent

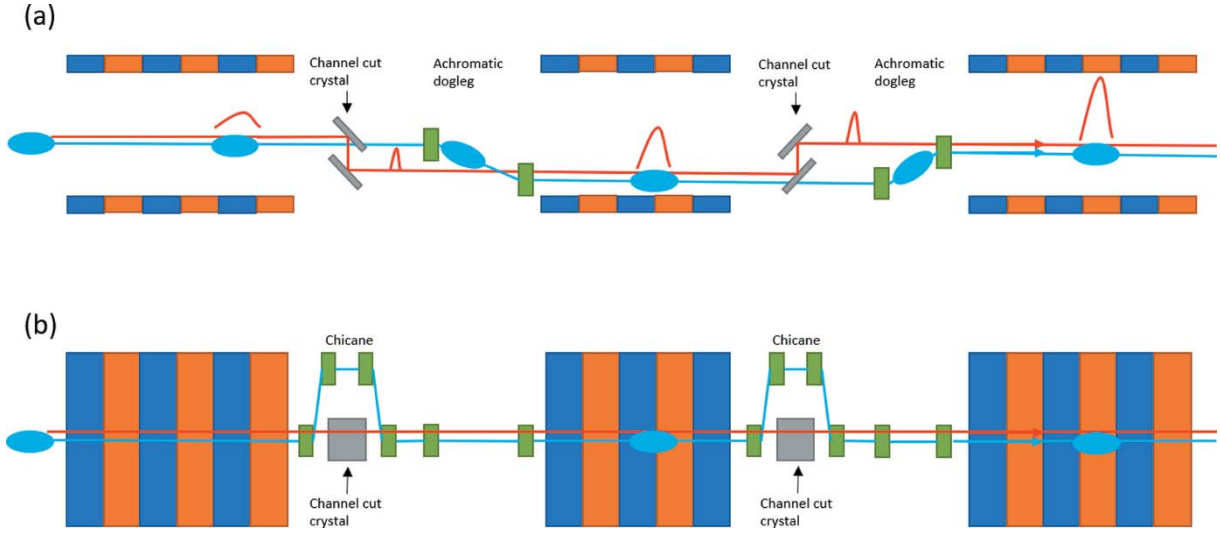

Figure 1
Two-stage reflective self-seeding configuration: (*a*) top view (*b*) side view.

FEL simulations. Two typical cases have been studied. One is with the FEL photon energy set to 4.5 keV, close to the lowest photon energy of the hard X-ray self-seeding operation; and the other is 9.5 keV, close to the highest photon energy for LCLS-II High Energy Upgrade (LCLS-II-HE) operation (Raubenheimer, 2018).

Through these simulations we will observe the evolution of the average FEL pulse energy and power spectrum. The undulator system configuration is optimized by revising the LCLS-II-HE baseline. In total, there are 32 slots in which the 8th and the 16th are replaced with chicanes, and the 9th and the 17th are reserved for doglegs. The remaining ones are variable gap undulators, with $\lambda_u = 2.6$ cm. For the 9.5 keV case, all undulators are enabled, but, for the 4.5 keV case, since the gain length is much shorter than that of the 9.5 keV case, to avoid early FEL saturation, we must disable several undulators in the second undulator section. The electron beam energy is set at 8 GeV and the current is 1.3 kA. Detailed information of the electron beam parameters is shown in Table 1. As shown in Table 2, we always choose Si(111) as the the first monochromator as the preliminary spectrum filter, so that we can generate a relatively wide bandwidth seed. In the 9.5 keV case, we choose Si(004) as the second monochromator to generate a narrow-bandwidth seed. In the 4.5 keV case, we choose Si(311) instead. The reflectivity and absorption curves of each one are shown in Fig. 2, which are calculated based on dynamic diffraction theory and equation (6), in which the input parameter are from *X-ray Server* (Stepanov, 1997). Notice that, since the thickness of the silicon used to manufacture the micro channel-cut monochromator is thick (500 µm), much longer than the absorption length, the transmission is almost zero.

We employ *Genesis 1.3* (Reiche, 1999), a 3D time-dependent FEL simulation code to demonstrate our idea. Based on the simulation, we find that in order to capture well the stochastic nature of a SASE FEL, we need to run 25 simulations with different initial electron beam shot noise for each photon energy. In these FEL simulations, the monochromators are made by perfect crystals. Later in this section, we will demonstrate that one can effectively suppress the heat load by cryo-cooling.

Table 1
Key parameters of the electron beam.

Parameters	Symbol	Value	Unit
Energy	E	8.00	GeV
Current	I	1300	A
Normalized emittance	$\gamma_0 \epsilon_{x,y}$	0.35	µm rad
Relative energy spread	σ_δ	0.01243%	a.u.
Core part duration	ΔT	10	fs
Repetition rate	f	300	kHz

Table 2
Key parameters of the micro channel-cut monochromator.

	9.5 keV	4.5 keV
First mono atomic layer	Si(111)	Si(111)
First mono Bragg angle	12.012	26.063
Second mono atomic layer	Si(004)	Si(311)
Second mono Bragg angle	28.726	57.278

For the 9.5 keV case, the seed performance for a TRSS scheme is shown in Fig. 3. Figs. 3(*a*) and 3(*b*) show the spectrum impinging on the first reflection point of the first and second micro channel-cut monochromator, respectively. The spectrum-domain profile in Figs. 3(*c*) and 3(*d*) shows that there are more modes going through the first monochromator, which is consistent with the fact that the first monochromator has a wider bandwidth than the second one. We also can observe this in the time domain shown in Figs. 3(*e*) and 3(*f*). The comparison of SASE and TRSS at 9.5 keV is shown in Fig. 4. From Figs. 4(*a*) and 4(*b*), we can find that the SASE and TRSS schemes have similar saturation power, and to achieve saturation they need almost the same number of undulators enabled. By comparing Figs. 4(*c*) and 4(*d*), it is clear that the TRSS scheme has a much narrower bandwidth than SASE, around a factor of nine. Hence, two-stage reflective self-seeding has a strong advantage with respect to spectrum brightness.

For the 4.5 keV case, the seed quality can be found in Fig. 5. The comparison between SASE and TRSS can be found in Fig. 6. The slippage effect in the 4.5 keV case is much stronger than that in the 9.5 keV case and the slippage effect helps to narrow the SASE FEL bandwidth (Bonifacio *et al.*, 1994). Thus, the spectrum brightness improvement is not as efficient as the 9.5 keV case. It is about five times better than the SASE.

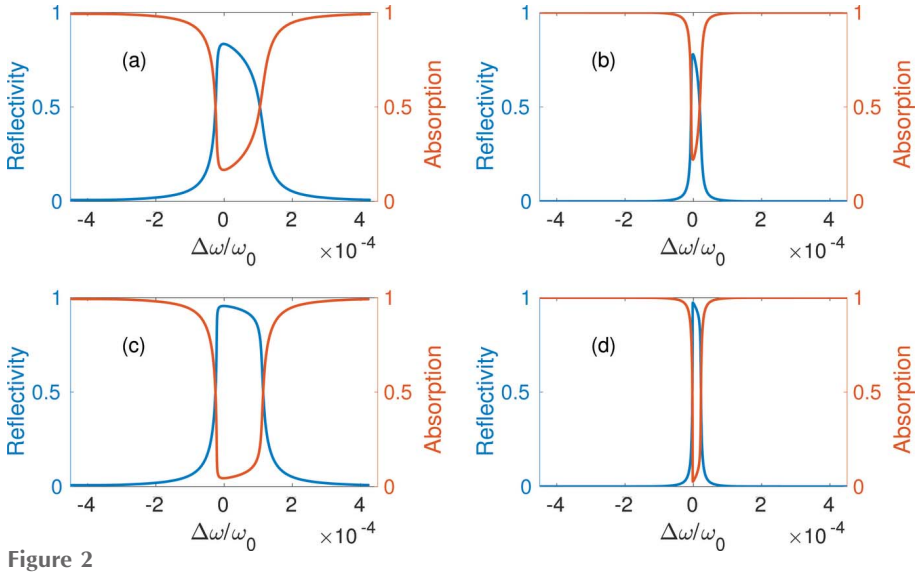

Figure 2
Reflectivity and absorption curves of given atomic layers and photon energies: (*a*) Si(111) with 4.5 keV X-rays; (*b*) Si(311) with 4.5 keV X-rays; (*c*) Si(111) with 9.5 keV X-rays; (*d*) Si (004) with 9.5 keV X-rays.

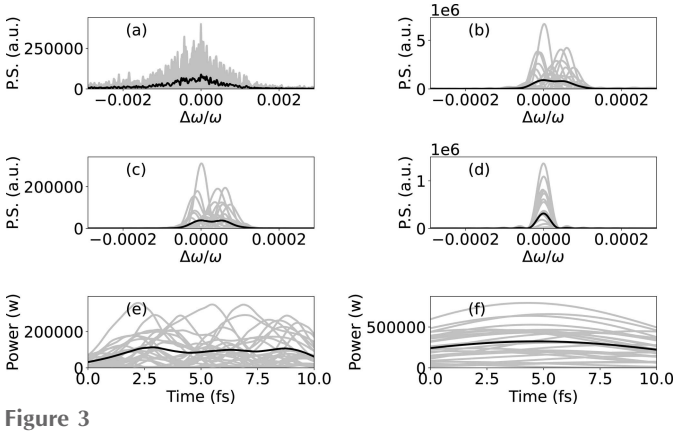

Figure 3
Seed performance of the 9.5 keV case. Gray lines indicate each shot starting from different initial electron beam shot-noise and black lines show the average seeds: (*a*) the spectrum impinging on the first reflection point of the first monochromator; (*b*) the spectrum impinging on the first reflection point of the second monochromator; (*c*) spectrum-domain seed profile after the first monochromator; (*d*) spectrum-domain seed profile after the second monochromator; (*e*) time-domain seed profile after the first monochromator; and (*f*) time-domain seed profile after the second monochromator. P.S. = power spectrum.

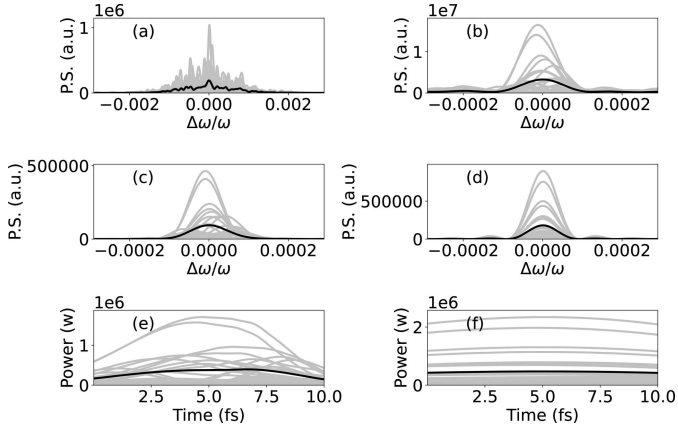

Figure 5
Seed performance of the 4.5 keV case. Gray lines indicate each shot with a different initial electron beam noise and black lines show the average seed: (*a*) the spectrum impinging on the first reflection point of the first monochromator; (*b*) the spectrum impinging on the first reflection point of the second monochromator; (*c*) spectrum-domain seed profile after the first monochromator; (*d*) spectrum-domain seed profile after the second monochromator; (*e*) time-domain seed profile after the first monochromator; and (*f*) time-domain seed profile after the second monochromator. P.S. = power spectrum.

Here, we show that the thermal load effects under the designed operation conditions can be effectively suppressed if the micro channel-cut monochromator is cryogenically cooled. We verify this by conducting finite-element analysis (FEA) using *COMSOL Multiphysics* software. To avoid excessive computational load, we simplify the periodic pulse heating by a quasi-continuous heating as shown in previous studies (Liu *et al.*, 2019), even though a pulse-by-pulse simulation can be performed by iteratively carrying out the procedure described in our previous work (Qu *et al.*, 2020*b*). The quasi-continuous analysis can significantly decrease the computational load, even though it tends to overestimate the residual strain compared with a pulse-by-pulse simulation. In fact it can give the actual design some safety margin, if the quasi-continuous analysis can satisfy the requirements.

The computational domain and corresponding boundary conditions are given in Fig. 7. Only the first reflection crystal is simulated because it absorbs around 85% heat load as compared with about 7% on the second reflection. The geometry of the monochromator is similar to the micro channel-cut monochromator used in SACLA hard X-ray self-seeding operation (Inoue *et al.*, 2019), but the lower part of the crystal is removed and replaced with a thermal insulation to improve computational efficiency. Such a simplification, again, introduces an overestimation of the residual thermally induced strain because one would expect considerable heat dissipation through this part. All surfaces in contact with metal parts [shown in Fig. 2(*b*) of Osaka *et al.* (2019)] are assumed to be cooled to 123 K (near the zero thermal expansion point of silicon) and fixed in normal direction. All other surfaces (top,

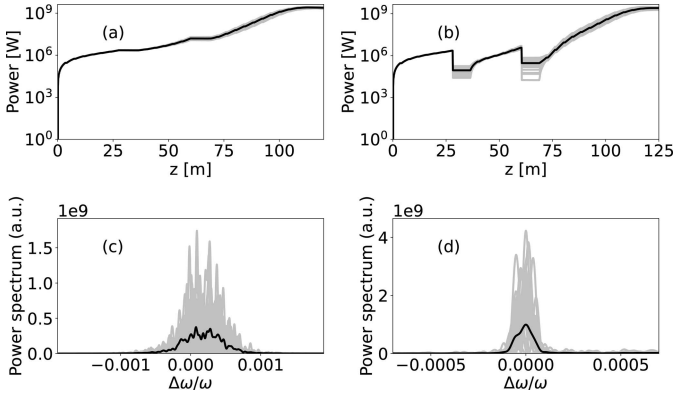

Figure 4
Performance comparison between SASE and TRSS with photon energy at 9.5 keV. Gray lines are the result of each shot with a different initial electron beam noise and black lines show the average result. (*a*) SASE FEL gain curve; (*b*) TRSS FEL gain curve; (*c*) SASE FEL spectrum around saturation; and (*d*) TRSS FEL spectrum around saturation.

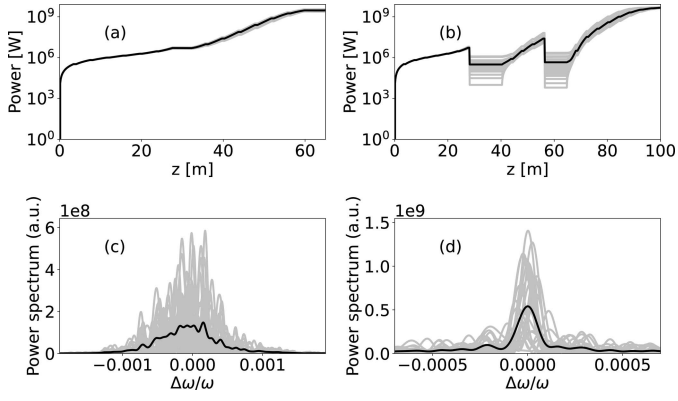

Figure 6
Performance comparison between SASE and TRSS with photon energies at 4.5 keV. Gray lines are the result of each shot with a different initial electron beam noise and black lines show the average result. (*a*) SASE FEL gain curve; (*b*) TRSS FEL gain curve; (*c*) SASE FEL spectrum around saturation; and (*d*) TRSS FEL spectrum around saturation.

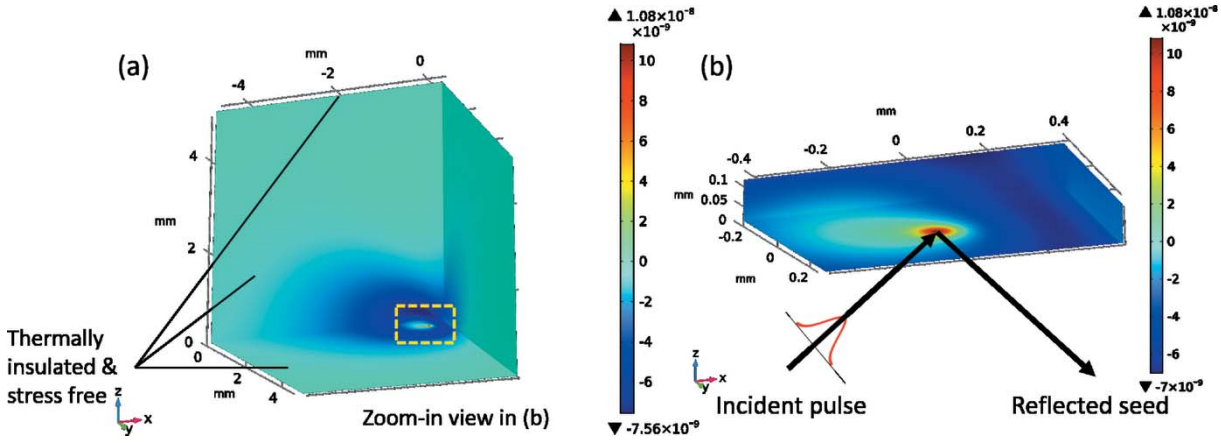

Figure 7
(*a*) Residual strain field for the first crystal in the second stage at 4.5 keV under heat load and (*b*) a zoom-in view near the XFEL footprint. The top, front and bottom surfaces are assumed thermally insulated and free of stress. All other surfaces are at constant temperature of 123 K and fixed in normal direction to simulate the mounting.

Table 3
Key inputs of the thermal mechanical simulation.

	9.5 keV	4.5 keV	
First mono FEL absorption	0.023	0.055	μJ
First mono spontaneous emission absorption	2.96	7.77	μJ
Second mono FEL absorption	0.037	0.25	μJ
Second mono spontaneous emission absorption	2.53	6.52	μJ

front and bottom) are assumed to be thermally insulated and free of stress. The FEL spot size (FWHM) is about 50 μm and the spontaneous emission spot size (FWHM) is about 1 mm. In addition, we summarize the key parameters for thermal mechanical simulations in Table 3.

The results of maximal strain in 3σ transverse XFEL footprint are summarized in Table 3. Among all cases, the maximal residual strain, even if overestimated by multiple simplifications, remains negligible (7.06×10^{-9}) compared with the Darwin width. This is attributed to (1) the superior thermal properties of silicon at cryogenic temperatures, especially near the zero thermal expansion point around 123 K, and (2) well controlled incident pulse energy, thanks to a high seeding efficiency (the pulse energy ratio between the seed and incident beam) of a reflective monochromator. Therefore, the crystal is able to avoid the thermal deformation as well as the resulted spectrum mismatch. Furthermore, in reality one should expect an even smaller impact, since the thermal load effect is overestimated in the simulation, as stated previously. Notice that this method can be further extended to the case for an electron beam with higher power, *e.g.* the European XFEL, by lowering the cooling temperature, which is straightforward for typical liquid-nitrogen cooling.

It is also worth pointing out that the cooling device for the reflective monochromator is easier to design as compared with the counterpart for transmissive monochromator. The transmissive monochromator is usually a thin diamond crystal and vulnerable to the internal strain due to even very minor external contact. On the contrary, the large crystal size in the reflective monochromator indicates much stronger resistance to strain by external force, which is a significant benefit for cooling implementation. On the other hand, it is difficult to implement a two-color self-seeding scheme (Lutman *et al.*, 2014) with the reflective-type monochromator.

4. Conclusion and outlook

A new scheme for solving the thermal load problem of a self-seeding FEL operated under high repetition rate has been proposed. We numerically demonstrated that the two-stage reflective self-seeding scheme has a clear advantage on mitigating the thermal load on the monochromator, so that the narrow spectrum of the output X-ray pulse can be preserved well. To fully explore the potential of this scheme, one can consider the crystal detuning effect and taper optimization to generate high-performance FEL pulses (Yang *et al.*, 2019; Jiao *et al.*, 2012; Tsai *et al.*, 2019). Also, one can consider using diamond to build artificial micro channel-cut monochromator to perform the TRSS scheme to reach higher seeding efficiency. In the future work, we will further investigate these topics.

Acknowledgements

The authors would like to thank the LCLS operation group for their dedicated support. The authors thank Diling Zhu, Zhibin Sun and Aaron Holman for their useful discussion and comments. The work was supported by the US Department of Energy (DOE) under contract DE-AC02-76SF00515 and the US DOE Office of Science Early Career Research Program grant FWP-2013-SLAC-100164.

Funding information

Funding for this research was provided by: the US Department of Energy (DOE) (contract No. DE-AC02-76SF00515); the US DOE Office of Science (award No. FWP-2013-SLAC-100164 to Juhao Wu).

References

Amann, J., Berg, W., Blank, V., Decker, F.-J., Ding, Y., Emma, P., Feng, Y., Frisch, J., Fritz, D., Hastings, J., Huang, Z., Krzywinski, J., Lindberg, R., Loos, H., Lutman, A., Nuhn, H.-D., Ratner, D., Rzepiela, J., Shu, D., Shvyd'ko, Y., Spampinati, S., Stoupin, S., Terentyev, S., Trakhtenberg, E., Walz, D., Welch, J., Wu, J., Zholents, A. & Zhu, D. (2012). *Nat. Photon.* **6**, 693–698.

Andruszkow, J., Aune, B., Ayvazyan, V., Baboi, N., Bakker, R., Balakin, V., Barni, D., Bazhan, A., Bernard, M., Bosotti, A., Bourdon, J. C., Brefeld, W., Brinkmann, R., Buhler, S., Carneiro, J., Castellano, M., Castro, P., Catani, L., Chel, S., Cho, Y., Choroba, S., Colby, E. R., Decking, W., Den Hartog, P., Desmons, M., Dohlus, M., Edwards, D., Edwards, H. T., Faatz, B., Feldhaus, J., Ferrario, M., Fitch, M. J., Flöttmann, K., Fouaidy, M., Gamp, A., Garvey, T., Gerth, C., Geitz, M., Gluskin, E., Gretchko, V., Hahn, U., Hartung, W. H., Hubert, D., Hüning, M., Ischebek, R., Jablonka, M., Joly, J. M., Juillard, M., Junquera, T., Jurkiewicz, P., Kabel, A., Kahl, J., Kaiser, H., Kamps, T., Katelev, V. V., Kirchgessner, J. L., Körfer, M., Kravchuk, L., Kreps, G., Krzywinski, J., Lokajczyk, T., Lange, R., Leblond, B., Leenen, M., Lesrel, J., Liepe, M., Liero, A., Limberg, T., Lorenz, R., Hua, L. H., Hai, L. F., Magne, C., Maslov, M., Materlik, G., Matheisen, A., Menzel, J., Michelato, P., Möller, W., Mosnier, A., Müller, U., Napoly, O., Novokhatski, A., Omeich, M., Padamsee, H. S., Pagani, C., Peters, F., Petersen, B., Pierini, P., Pflüger, J., Piot, P., Phung Ngoc, B., Plucinski, L., Proch, D., Rehlich, K., Reiche, S., Reschke, D., Reyzl, I., Rosenzweig, J., Rossbach, J., Roth, S., Saldin, E. L., Sandner, W., Sanok, Z., Schlarb, H., Schmidt, G., Schmüser, P., Schneider, J. R., Schneidmiller, E. A., Schreiber, H., Schreiber, S., Schütt, P., Sekutowicz, J., Serafini, L., Sertore, D., Setzer, S., Simrock, S., Sonntag, B., Sparr, B., Stephan, F., Sytchev, V. A., Tazzari, S., Tazzioli, F., Tigner, M., Timm, M., Tonutti, M., Trakhtenberg, E., Treusch, R., Trines, D., Verzilov, V., Vielitz, T., Vogel, V., Walter, G., **v**, Wanzenberg, R., Weiland, T., Weise, H., Weisend, J., Wendt, M., Werner, M., White, M. M., Will, I., Wolff, S., Yurkov, M. V., Zapfe, K., Zhogolev, P. & Zhou, F. (2000). *Phys. Rev. Lett.* **85**, 3825–3829.

Bonifacio, R., De Salvo, L., Pierini, P., Piovella, N. & Pellegrini, C. (1994). *Phys. Rev. Lett.* **73**, 70–73.

Bonifacio, R., Pellegrini, C. & Narducci, L. (1984). *Opt. Commun.* **50**, 373–378.

Decking, W. *et al.* (2020). *Nat. Photon.* **14**, 391–397.

Emma, P., Akre, R., Arthur, J., Bionta, R., Bostedt, C., Bozek, J., Brachmann, A., Bucksbaum, P., Coffee, R., Decker, F.-J., Ding, Y., Dowell, D., Edstrom, S., Fisher, A., Frisch, J., Gilevich, S., Hastings, J., Hays, G., Hering, P., Huang, Z., Iverson, R., Loos, H., Messerschmidt, M., Miahnahri, A., Moeller, S., Nuhn, H.-D., Pile, G., Ratner, D., Rzepiela, J., Schultz, D., Smith, T., Stefan, P., Tompkins, H., Turner, J., Welch, J., White, W., Wu, J., Yocky, G. & Galayda, J. (2010). *Nat. Photon.* **4**, 641–647.

Emma, P., Frisch, J., Huang, Z., Marinelli, A., Maxwell, T., Loos, H., Nosochkov, Y., Raubenheimer, T., Welch, J., Wang, L., Woodley, M., Saini, A., Solyak, N., Qiang, J. & Venturini, M. (2014). *Proceedings of the 36th International Free-Electron Laser Conference (FEL2014)*, 25–29 August 2014, Basel, Switzerland, p. 743.

Geloni, G., Kocharyan, V. & Saldin, E. (2011). *arXiv*:1109.5112.

Inoue, I., Osaka, T., Hara, T., Tanaka, T., Inagaki, T., Fukui, T., Goto, S., Inubushi, Y., Kimura, H., Kinjo, R., Ohashi, H., Togawa, K., Tono, K., Yamaga, M., Tanaka, H., Ishikawa, T. & Yabashi, M. (2019). *Nat. Photon.* **13**, 319–322.

Ishikawa, T., Aoyagi, H., Asaka, T., Asano, Y., Azumi, N., Bizen, T., Ego, H., Fukami, K., Fukui, T., Furukawa, Y., Goto, S., Hanaki, H., Hara, T., Hasegawa, T., Hatsui, T., Higashiya, A., Hirono, T., Hosoda, N., Ishii, M., Inagaki, T., Inubushi, Y., Itoga, T., Joti, Y., Kago, M., Kameshima, T., Kimura, H., Kirihara, Y., Kiyomichi, A., Kobayashi, T., Kondo, C., Kudo, T., Maesaka, H., Maréchal, X. M., Masuda, T., Matsubara, S., Matsumoto, T., Matsushita, T., Matsui, S., Nagasono, M., Nariyama, N., Ohashi, H., Ohata, T., Ohshima, T., Ono, S., Otake, Y., Saji, C., Sakurai, T., Sato, T., Sawada, K., Seike, T., Shirasawa, K., Sugimoto, T., Suzuki, S., Takahashi, S., Takebe, H., Takeshita, K., Tamasaku, K., Tanaka, H., Tanaka, R., Tanaka, T., Togashi, T., Togawa, K., Tokuhisa, A., Tomizawa, H., Tono, K., Wu, S., Yabashi, M., Yamaga, M., Yamashita, A., Yanagida, K., Zhang, C., Shintake, T., Kitamura, H. & Kumagai, N. (2012). *Nat. Photon.* **6**, 540–544.

Jiao, Y., Wu, J., Cai, Y., Chao, A. W., Fawley, W. M., Frisch, J., Huang, Z., Nuhn, H.-D., Pellegrini, C. & Reiche, S. (2012). *Phys. Rev. ST Accel. Beams*, **15**, 050704.

Kang, H.-S., Min, C.-K., Heo, H., Kim, C., Yang, H., Kim, G., Nam, I., Baek, S. Y., Choi, H.-J., Mun, G., Park, B. R., Suh, Y. J., Shin, D. C., Hu, J., Hong, J., Jung, S., Kim, S.-H., Kim, K., Na, D., Park, S. S., Park, Y. J., Han, J.-H., Jung, Y. G., Jeong, S. H., Lee, H. G., Lee, S., Lee, S., Lee, W.-W., Oh, B., Suh, H. S., Parc, Y. W., Park, S.-J., Kim, M. H., Jung, N.-S., Kim, Y.-C., Lee, M.-S., Lee, B.-H., Sung, C.-W., Mok, I.-S., Yang, J.-M., Lee, C.-S., Shin, H., Kim, J. H., Kim, Y., Lee, J. H., Park, S.-Y., Kim, J., Park, J., Eom, I., Rah, S., Kim, S., Nam, K. H., Park, J., Park, J., Kim, S., Kwon, S., Park, S. H., Kim, K. S., Hyun, H., Kim, S. N., Kim, S., Hwang, S., Kim, M. J., Lim, C., Yu, C., Kim, B.-S., Kang, T.-H., Kim, K.-W., Kim, S.-H., Lee, H.-S., Lee, H.-S., Park, K.-H., Koo, T.-Y., Kim, D.-E. & Ko, I. S. (2017). *Nat. Photon.* **11**, 708–713.

Kondratenko, A. M. & Saldin, E. L. (1980). *Part. Accel.* **10**, 207–216.

Liu, S., Decking, W., Kocharyan, V., Saldin, E., Serkez, S., Shayduk, R., Sinn, H. & Geloni, G. (2019). *Phys. Rev. Accel. Beams*, **22**, 060704.

Lugovskaya, O. & Stepanov, S. (1991). *Sov. Phys. Crystallogr.* **36**, 478.

Lutman, A. A., Decker, F.-J., Arthur, J., Chollet, M., Feng, Y., Hastings, J., Huang, Z., Lemke, H., Nuhn, H.-D., Marinelli, A., Turner, J. L., Wakatsuki, S., Welch, J. & Zhu, D. (2014). *Phys. Rev. Lett.* **113**, 254801.

Milathianaki, D., Boutet, S., Williams, G. J., Higginbotham, A., Ratner, D., Gleason, A. E., Messerschmidt, M., Seibert, M. M., Swift, D. C., Hering, P., Robinson, J., White, W. E. & Wark, J. S. (2013). *Science*, **342**, 220–223.

Osaka, T., Inoue, I., Kinjo, R., Hirano, T., Morioka, Y., Sano, Y., Yamauchi, K. & Yabashi, M. (2019). *J. Synchrotron Rad.* **26**, 1496–1502.

Qu, Z., Ma, Y., Zhou, G. & Wu, J. (2020*a*). *Opt. Express*, **28**, 30075.

Qu, Z., Ma, Y., Zhou, G. & Wu, J. (2020*b*). *Nucl. Instrum. Methods Phys. Res. A*, **969**, 163936.

Raubenheimer, T. (2018). *Proceedings of the 60th ICFA Advanced Beam Dynamics Workshop on Future Light Sources (FLS2018)*, 5–9 March 2018, Shanghai, China, p. 6.

Reiche, S. (1999). *Nucl. Instrum. Methods Phys. Res. A*, **429**, 243–248.

Samoylova, L., Shu, D., Dong, X., Geloni, G., Karabekyan, S., Terentev, S., Blank, V., Liu, S., Wohlenberg, T., Decking, W. & Sinn, H. (2019). *AIP Conf. Proc.* **2054**, 030016.

Seibert, M. M., Ekeberg, T., Maia, F. R. N. C., Svenda, M., Andreasson, J., Jönsson, O., Odić, D., Iwan, B., Rocker, A., Westphal, D., Hantke, M., DePonte, D. P., Barty, A., Schulz, J., Gumprecht, L., Coppola, N., Aquila, A., Liang, M., White, T. A., Martin, A., Caleman, C., Stern, S., Abergel, C., Seltzer, V., Claverie, J.-M., Bostedt, C., Bozek, J. D., Boutet, S., Miahnahri, A. A., Messerschmidt, M., Krzywinski, J., Williams, G., Hodgson, K. O., Bogan, M. J., Hampton, C. Y., Sierra, R. G., Starodub, D., Andersson, I., Bajt, S., Barthelmess, M., Spence, J. C. H., Fromme, P., Weierstall, U., Kirian, R., Hunter, M., Doak, R. B., Marchesini, S., Hau-Riege, S. P., Frank, M., Shoeman, R. L., Lomb, L., Epp, S. W., Hartmann, R., Rolles, D., Rudenko, A., Schmidt, C., Foucar, L., Kimmel, N., Holl, P., Rudek, B., Erk, B., Hömke, A., Reich, C., Pietschner, D., Weidenspointner, G., Strüder, L., Hauser, G., Gorke, H., Ullrich, J., Schlichting, I., Herrmann, S., Schaller, G., Schopper, F., Soltau, H., Kühnel, K.-U., Andritschke, R., Schröter, C.-D., Krasniqi, F., Bott, M., Schorb, S., Rupp, D., Adolph, M.,

Gorkhover, T., Hirsemann, H., Potdevin, G., Graafsma, H., Nilsson, B., Chapman, H. N. & Hajdu, J. (2011). *Nature*, **470**, 78–81.
Shvyd'ko, Y. & Lindberg, R. (2012). *Phys. Rev. ST Accel. Beams*, **15**, 100702.
Stepanov, S. (1997). *X-ray server*, https://x-server.gmca.aps.anl.gov/.
Tsai, C.-Y., Emma, C., Wu, J., Yoon, M., Wang, X., Yang, C. & Zhou, G. (2019). *Nucl. Instrum. Methods Phys. Res. A*, **913**, 107–119.
Wu, J., Ding, Y., Emma, P., Huang, Z., Loos, H., Messerschmidt, M., Schneidmiller, E. & Yurkov, M. (2010). *Proceedings of the 32nd International Free Electron Laser Conference (FEL2010)*, 23–27 August 2010, Malmo, Sweden, p. 147. MOPC14F.
Yang, B., Wang, S. & Wu, J. (2018*a*). *J. Synchrotron Rad.* **25**, 166–176.
Yang, C., Tsai, C.-Y., Zhou, G., Wang, X., Hong, Y., Krug, E. D., Li, A., Deng, H., He, D. & Wu, J. (2019). *Opt. Express*, **27**, 13229–13239.
Yang, C., Wu, J., Zhou, G., Yang, B., Tsai, C.-Y., Yoon, M., Feng, Y. & Raubenheimer, T. (2018*b*). *Proceedings of the 38th International Free Electron Laser Conference (FEL2017)*, 20–25 August 2017, Santa Fe, NM, USA, p. 68. MOP018.
Young, L., Kanter, E. P., Krässig, B., Li, Y., March, A. M., Pratt, S. T., Santra, R., Southworth, S. H., Rohringer, N., DiMauro, L. F., Doumy, G., Roedig, C. A., Berrah, N., Fang, L., Hoener, M., Bucksbaum, P. H., Cryan, J. P., Ghimire, S., Glownia, J. M., Reis, D. A., Bozek, J. D., Bostedt, C. & Messerschmidt, M. (2010). *Nature*, **466**, 56–61.
Zhang, W., Alonso-Mori, R., Bergmann, U., Bressler, C., Chollet, M., Galler, A., Gawelda, W., Hadt, R. G., Hartsock, R. W., Kroll, T., Kjaer, K. S., Kubiček, K., Lemke, H. T., Liang, H. W., Meyer, D. A., Nielsen, M. M., Purser, C., Robinson, J. S., Solomon, E. I., Sun, Z., Sokaras, D., van Driel, T. B., Vankó, G., Weng, T.-C., Zhu, D. & Gaffney, K. J. (2014). *Nature*, **509**, 345–348.
Zhou, G., Decker, F.-J., Ding, Y., Jiao, Y., Lutman, A. A., Maxwell, T. J., Raubenheimer, T. O., Wang, J., Holman, A. J., Tsai, C.-Y., Wu, J. Y., Wu, W., Yang, C., Yoon, M. & Wu, J. (2020). *Sci. Rep.* **10**, 5961.